If several Regge poles with the same quantum numbers are considered, and if cuts and background integrals are included, then the $g(P,I;s)$ represent the total contribution of the Regge family with the given P and I. It is only in the high energy region that Eq. (29) might be expected to be adequate with just the highest ranking trajectory included.

The correspondence with the usual trajectory families is

$$g(+, 0) \rightarrow \text{Pomeranchuk family},$$
$$g(-, 0) \rightarrow \omega \text{ family},$$
$$g(-, 1) \rightarrow \rho \text{ family},$$

and

$$g(+, 1) \rightarrow R \text{ family}.$$

Note that of the twelve possible sets of trajectory quantum numbers for the $N\bar{N}$ system,[2] only the above four contribute to f_2 and therefore to the total s-channel cross sections. The R trajectory[5] has not usually been included in Regge-pole analyses, as there is no known resonance with its quantum number, $I(J^{PG}) = 1(J_{\text{even}}{}^{+-})$. However, in a systematic analysis it should be included, and Eqs. (24) would indicate whether its effect is negligible or not.

IV. CONCLUSION

The use of Eqs. (24) offers a simple and systematic scheme for analyzing theoretical models in terms of experimental total cross sections. The functions $g(P,I;s)$, constructed from the experimental cross sections, have a fundamental physical significance because they are directly related to one of the $N\bar{N} \rightarrow N\bar{N}$ spin-triplet amplitudes in a given state of parity P and isospin I.

It is hoped that the above-mentioned results will act as a spur toward the measurement of the $\bar{p}n$ or, equivalently, $\bar{n}p$ total cross sections.

ACKNOWLEDGMENT

The authors are indebted to Professor Geoffrey F. Chew for a stimulating discussion.

[5] A. Pignotti, Phys Rev. **134**, B630 (1964); A. Ahmadzadeh, Phys. Rev. **134**, B633 (1964).

Elastic Scattering of Positive Pions by Protons in the Energy Range 500–1600 MeV*

Jerome A. Helland, Thomas J. Devlin,† Donald E. Hagge, Michael J. Longo,‡
Burton J. Moyer, and Calvin D. Wood§

Lawrence Radiation Laboratory, University of California, Berkeley, California

(Received 13 January 1964)

Differential cross sections for the elastic scattering of positive pi mesons by protons were measured at the Berkeley Bevatron at pion laboratory kinetic energies between 500 and 1600 MeV. Fifty scintillation counters and a matrix coincidence system were used to identify incoming pions and detect the recoil proton and pion companions. Results were fitted with a power series in the cosine of the center-of-mass scattering angle, and total elastic cross sections were obtained by integrating under the fitted curves. The coefficients of the cosine series are displayed, plotted versus the laboratory kinetic energy of the pion. The most striking features of these curves are the large positive value of the coefficient of $\cos^6\theta^*$, and the large negative value of the coefficient of $\cos^4\theta^*$, both of which maximize in the vicinity of the 1350-MeV peak in the total cross section. These results indicate that the most predominant state contributing to the scattering at the 1350-MeV peak has total angular momentum $J = \frac{7}{2}$, since the coefficients for terms above $\cos^6\theta^*$ are negligible at this energy. One possible explanation is that the 1350-MeV peak is the result of an $F_{7/2}$ resonance lying on the same Regge-pole trajectory as the $(\frac{3}{2}, \frac{3}{2})$ resonance near 195 MeV.

I. INTRODUCTION

THIS experiment constitutes a portion of an extensive study of the phenomenology of the $\pi - N$ interaction in the energy region above the well-known $(\frac{3}{2}, \frac{3}{2})$ resonance occurring at the pion kinetic energy of 195 MeV (≈ 1236-MeV total c.m. energy for the $\pi - N$ system). The features of outstanding interest are indicated by the cross-section variations displayed in Fig. 1, based on measurements by several experimental groups.[1]

[1] See for example: H. C. Burrowes, D. O. Caldwell, D. H. Frisch, D. A. Hill, D. M. Ritson, R. A. Schulter, and M. A. Wahlig, Phys. Rev. Letters **2**, 119 (1959); T. J. Devlin, B. J. Moyer, and V. Perez-Mendez, Phys. Rev. **125**, 690 (1962); J. C. Brisson, J. F. Detoeuf, P. Falk-Vairant, L. Van Rossum, and G. Valladas, Nuovo Cimento **19**, 210 (1961); M. J. Longo, J. A. Helland, W. N. Hess, B. J. Moyer, and V. Perez-Mendez, Phys. Rev. Letters **3**, 568 (1959).
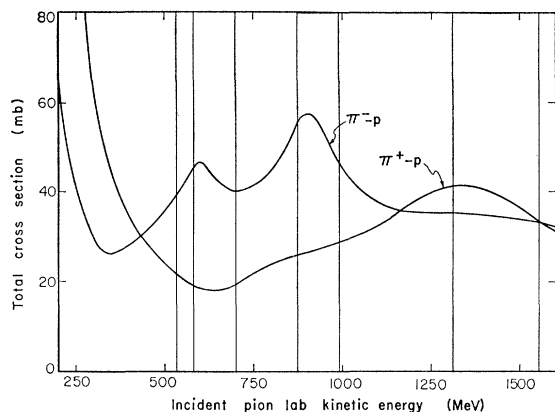
FIG. 1. Total cross sections for $\pi^{\pm}-p$ scattering, showing the energies at which differential cross sections were measured in this experiment.

A measurement of the π^--p differential cross sections has been reported by this same research group.[2] The energies chosen for the present π^+-p measurements, in which only the $\frac{3}{2}$ state of isotopic spin appears, agreed with those of our π^--p work so as to assist in the decomposition of that data into its $\frac{3}{2}$ and $\frac{1}{2}$ isotopic spin-state components.

The present experiment is furthermore intended to supply data necessary for the characterization of the interaction in the region of the broad peak in the π^+-p cross section observed at about 1350-MeV pion energy (1920-MeV total c.m. energy), and in the "shoulder" on the low-energy side of the peak. The shoulder is tentatively considered to indicate the maximizing of a partial cross-section contribution at about 850 MeV.

Although considerable work has been done in the study of π^--p scattering, less has been done on π^+-p scattering in this energy range. Several bubble-chamber experiments have been performed within the past few years to measure the π^+-p differential cross sections (d.c.s.). Bidan et al., using the Saclay propane bubble chamber, measured the d.c.s. at 1000 MeV.[3] Barloutaud et al., using the Saclay hydrogen bubble chamber, measured the d.c.s. at 820, 900, and 1050 MeV.[3] Kopp et al., using a hydrogen bubble chamber at the Brookhaven Cosmotron, measured the d.c.s. at 990 MeV.[3] Roellig and Glaser, using a propane bubble chamber at Michigan, measured the d.c.s. at 1100 MeV.[3] (This work is also discussed by Malenka and Valk.[3]) Willis, using a

hydrogen bubble chamber at Brookhaven, measured the d.c.s. at 500 MeV.[3] In most of these experiments the π^+-p d.c.s. is based on 200–1200 events per energy.

It may be desirable to characterize the $\pi-p$ scattering in terms of phase shifts. However, with only the differential elastic, total elastic, and total cross sections available, it is impossible in principle to determine all the phase shifts, because the existence of nonelastic processes causes them to be complex, and thus doubles the number of parameters to be determined. It is necessary to provide the further constraints of polarization data for the recoil protons, and differential elastic charge-exchange cross sections in the π^--p case, before any reasonable expectation of phase-shift determinations can be entertained. Such measurements are in fact in progress. An extensive phase-shift search program has been developed by Cence for digital computation of phase-shift sets.[4]

Even short of complete knowledge of the phase shifts it may be possible to qualitatively distinguish between cross-section peaks due to a state in resonance superimposed upon a nonresonant background, and a peak which may be the result of a rapidly increasing inelastic cross section rising to the limit imposed by unitarity. A form of this latter mechanism has been proposed by Ball and Frazer.[5]

Since all strong interactions are tentatively believed to be related, a thorough knowledge of the $\pi-p$ interaction should be helpful in achieving understanding of the phenomena observed in the $K-N$ and π-hyperon systems. Our first effort is to identify quantum numbers for the interactions contributing to the phenomena indicated by the cross-section variations.

II. EXPERIMENTAL METHOD AND EQUIPMENT

A. Experimental Method

A beam of positive pions of selected momentum was focused with small angular convergence on a liquid-hydrogen (LH₂) target. The differential cross sections for the elastic scattering of the pions were measured by detecting the scattered pions and their companion recoil protons in the proper time relationship with the incident pions. Scintillation counters in an extensive array were used as detectors.

The detection of inelastic scattering events in the elastic-scattering channels was minimized by the geometrical restrictions of related pion and proton counters. This method was used rather than one involving Čerenkov counters, or range telescopes, etc., because it accomplished its purpose adequately and it avoided the difficult corrections due to Čerenkov-counter inefficiencies, or scattering in a range telescope, which must be applied when using those methods. A sampling of the inelastic scattering was taken in several counter pairs

[2] C. D. Wood, T. J. Devlin, J. A. Helland, M. J. Longo, B. J. Moyer, and V. Perez-Mendez, Phys. Rev. Letters 6, 481 (1961). J. A. Helland, T. J. Devlin, D. E. Hagge, M. J. Longo, B. J. Moyer, V. Perez-Mendez, and C. D. Wood, following article, Phys. Rev. 134, B1079 (1964).

[3] U. Bidan, F. Levy, N. Abbattista, A. Minafra, S. Mongelli, A. Romano, and P. Waloschek, Nuovo Cimento 24, 334 (1962); R. Barloutaud, C. Choquet-Louedec, A. Derem, J. Heughebaert, A. Leveque, and J. Meyer, Phys. Rev. Letters 1, 207 (1962); J. K. Kopp, A. M. Shapiro, and A. R. Erwin, Phys. Rev. 123, 301 (1961); L. O. Roellig and D. A. Glaser, ibid. 116, 1001 (1959); B. J. Malenka and H. S. Valk, ibid. 122, 934 (1961); W. J. Willis, ibid. 116, 753 (1959).

[4] R. J. Cence, formerly of this Laboratory, now at the University of Hawaii, Honolulu (private communication).

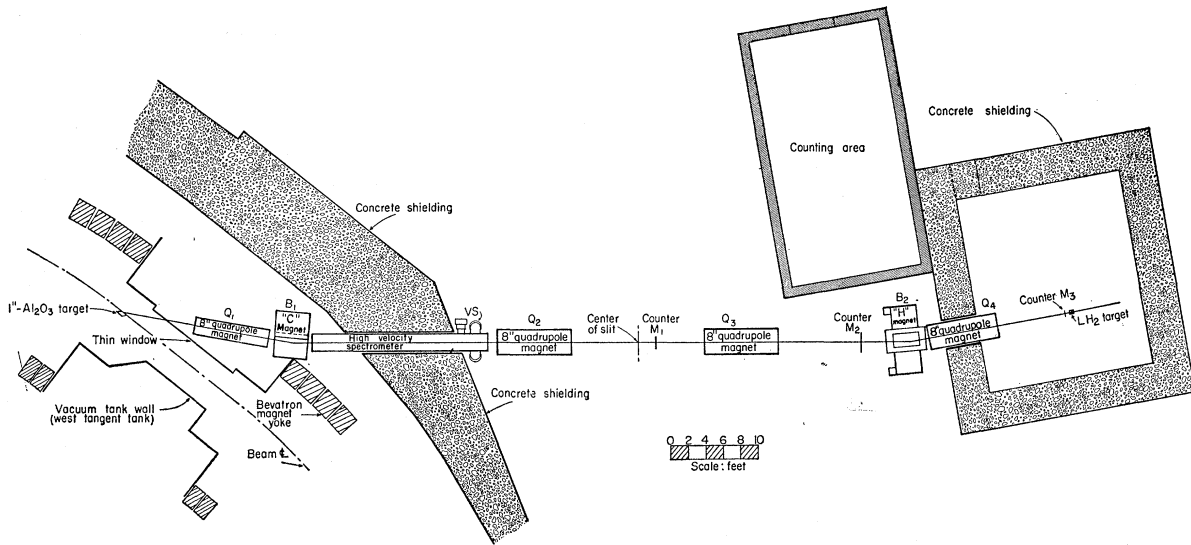[5] J. S. Ball and W. R. Frazer, Phys. Rev. Letters 7, 204 (1961).

FIG. 2. Plan view of the experimental arrangement. The counters, the LH₂ target, and the Al₂O₃ target are not drawn to scale.

not elastically related, in order to correct the elastic data for inelastic events. This is explained in more detail in Sec. III B along with other corrections. Differential cross sections at lab pion scattering angles smaller than about 20 deg could not be measured, because for those events the recoil proton did not have enough energy to reach the proton detectors and be counted.

The precise values of the pion lab kinetic energies at the scattering target were 533, 581, 698, 873, 990, 1311, and 1555 MeV, as determined by weighted means of values obtained from wire-orbit measurements, time-of-flight measurements, gas Čerenkov-counter pressure curves, velocity-spectrometer data, and beam-focusing data. The wire-orbit and time-of-flight measurements were of course given principal weight.

A plan view of the beam transport components is given in Fig. 2, which also indicates the positions of the beam monitor counters M_1, M_2 and M_3. The purpose

of the velocity spectrometer (or selector) was to suppress the proton component of the beam. The muon and electron beam contamination was measured at various energies by a gas Čerenkov counter.

B. Pion Source, Beam Design, and Hydrogen Target

The pions were produced in a ceramic target of aluminum oxide traversed by the Bevatron proton beam. It was desirable to achieve high nucleon density—but low nuclear mass number—in such a target in order to maximize the effective pion-producing nucleon collisions. Also a low atomic number was desired here so as to suppress the positron contamination of the pion beam deriving from π^0 production and decay with subsequent conversion of the decay photons in the target material. The Al₂O₃, fabricated with a density of about
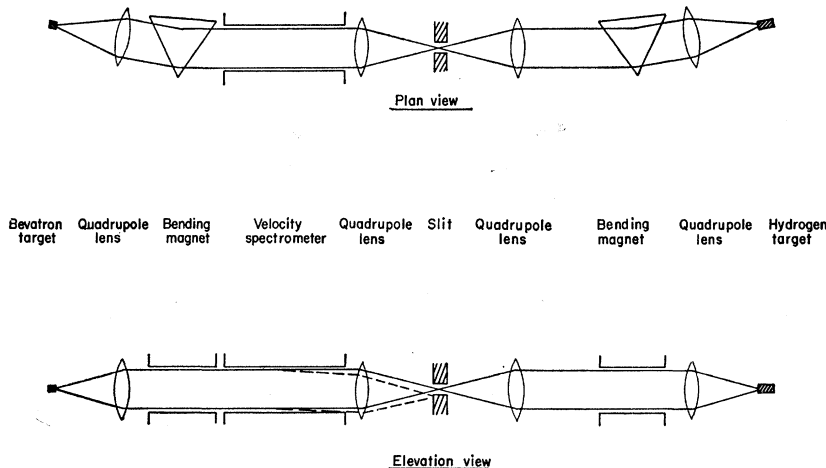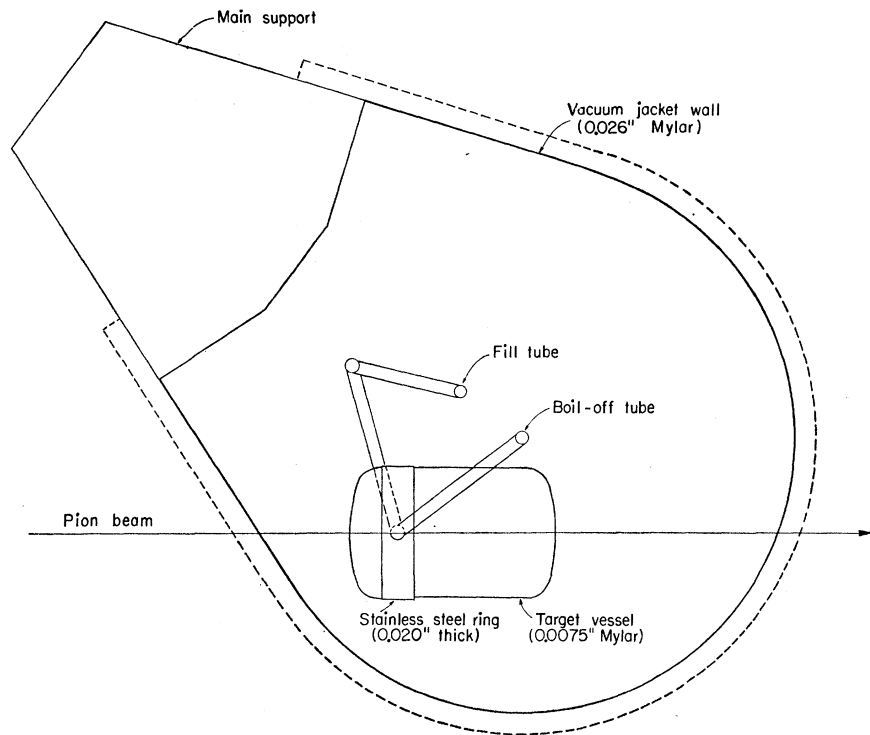

FIG. 3. Schematic diagram of optical system showing extreme rays of pion beam, various magnets, targets, slit, and velocity spectrometer. The dashed lines illustrate how the protons were stopped by the slit.

FIG. 4. Plan view of liquid-hydrogen target vessel and surrounding vacuum-jacket wall.

4 g/cm³, was a suitable compromise of these requirements. It was of such a size as to constitute an "object" $\frac{1}{2}$ in. wide and $\frac{1}{8}$ in. high as viewed by the pion-beam optical system. The proton-beam path through the target was about 1 in. in length, due to the oblique orientation of the ceramic bar relative to the proton beam.

The proton beam pulses, typically of about 10^{11} protons, were delivered ten times per min, each pulse being spread as uniformly as possible over a time interval of 0.2 sec. The associated pion-beam pulses ranged from 10^4 to 3×10^4, depending upon the momentum selected.

The pion-beam design is schematically shown in Fig. 3. A focus in both horizontal and vertical planes was produced at the slit. In the horizontal plane there was a continuous distribution of images of the Bevatron target because of the momentum dispersion induced by the first bending magnet. The slit, designed of thick copper bars, selected a momentum band of $\pm 3\%$, which was nearly recombined at the final image position by the action of the second bending magnet.

In addition to selecting the momentum band by horizontal definition of the beam, the slit—by its vertical definition—served to remove the protons that were deflected downward by the velocity selector to an image position below the beam axis, as shown in Fig. 3. Use of the velocity selector reduced the proton/pion ratio from ≈ 15 to ≈ 3 at the highest beam energy; at the lowest energy the final ratio was 0.02. Those protons not thus eliminated were rejected by the time-of-flight condition. Indeed, the velocity selector was not at all

necessary for this experiment; it was incorporated into the system only to reduce the unwanted proton flux.

The LH₂ target is shown in plan view in Fig. 4. The target vessel was a Mylar cylinder $2\frac{1}{2}$ in. in diameter and 4 in. long, surrounded by radiation shields of aluminized Mylar to minimize heat transfer to the LH₂. The vessel was filled by gravity feed from a reservoir surrounded by a liquid-nitrogen jacket. The entire assembly was enclosed in a vacuum jacket. The target vessel was emptied by closing its boil-off valve, thereby building up a slight gas pressure and forcing the LH₂ out the bottom fill tube and up into the reservoir. The density[6]
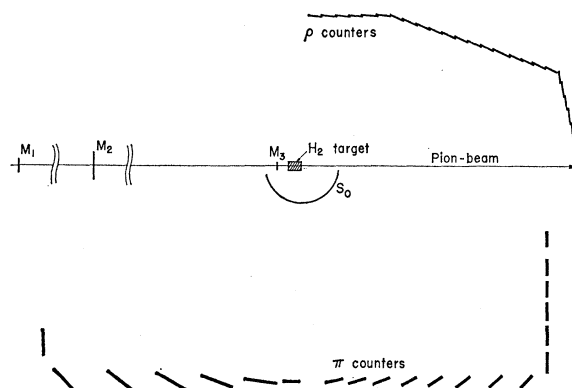

FIG. 5. Plan view of scintillation-counter arrangement.

[6] D. B. Chelton and D. B. Mann, University of California Radiation Laboratory Report UCRL-3421, 1956 (unpublished).
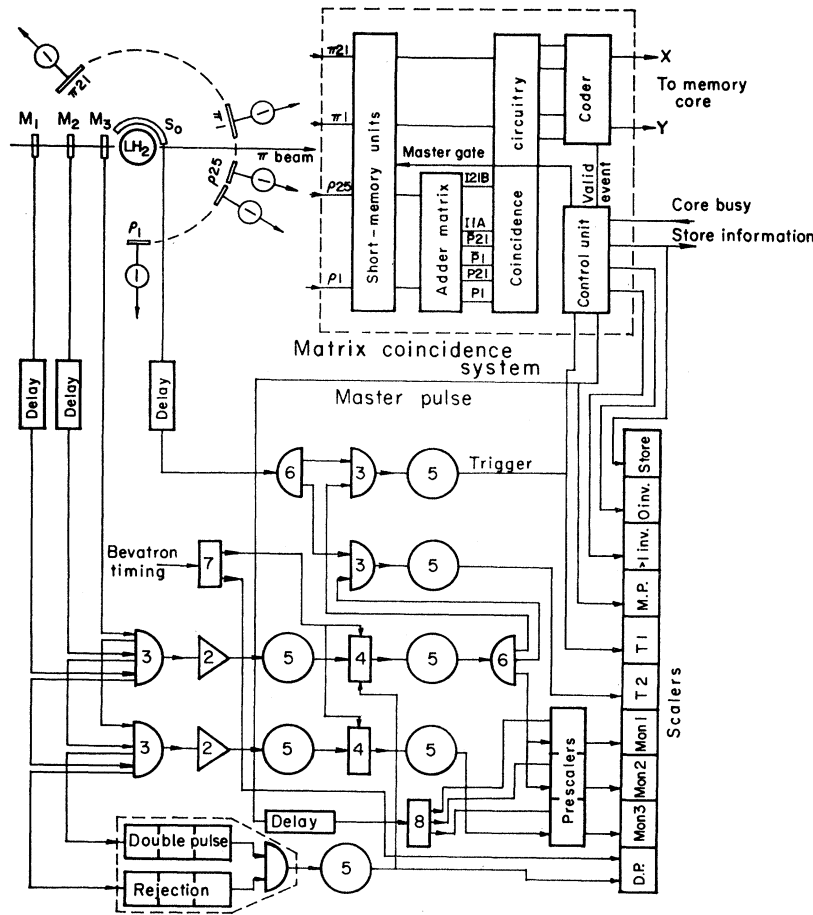
Fig. 6. Block diagram of electronics: 1. tunnel-diode pulse discriminator and shaper; 2. fast amplifier; 3. fast coincidence circuit; 4. gate circuit; 5. pulse-amplitude discriminator; 6. pulse splitter; 7. scaler gate and beam monitor with modified output; 8. special gate circuit used to turn off prescalers during time data storage system is busy.

of the gaseous hydrogen left in the target was 0.00136 g/cm³, whereas the density of the LH₂ is only 0.0702 g/cm³; this required a 2% correction to be applied to the amount of LH₂.

The effective number of protons per cm² was calculated to be 4.196×10^{23}. This value includes the 2% density correction, and takes into consideration the shape of the target vessel, and the beam profile (relative intensity of the pion beam for positions off the central beam axis).

C. Scintillation Counter Array

Figure 5 shows the entire counter array schematically. Three counters (M_1, M_2, and M_3) were used to count those pions, incident on the LH₂ target, that could contribute to the scattering data. Counter M_3 was smaller in diameter than the target vessel, and served to define the accepted beam of particles so that none traversed the side walls of the vessel.

There were 21 pion counters, labeled "π counters," placed at various lab angles between 16 and 145 deg to the right of the beam, as viewed looking downstream. Twenty-five counters, labeled "ρ counters," were placed to the left of the beam at lab angles between 4 and 82

deg; these counters detected the protons as they recoiled from the $\pi - p$ elastic collisions. The ρ counters were added together electronically in overlapping groups of three to six counters. These groups of ρ counters were called "P counters." For each π counter there was a corresponding P counter. The P counter was slightly larger than necessary to detect the proton recoiling from any elastically scattered pion that was detected in the corresponding π counter.

The π counters were all designed to subtend an angle of 18 deg in ϕ, the azimuthal angle in a spherical-coordinate system. The 25 ρ counters, which detected the recoil protons, were designed to subtend an angle $\phi \approx 22$ deg.

As was indicated above, the π counters defined the scattering angles and solid angles. The cosines of the effective c.m. scattering angles, and the c.m. solid angles subtended, were carefully evaluated for each π counter at each experimental energy; but in the interest of brevity these values are not listed here. The magnitudes of solid angles ranged between 3 and 36 msr, and the breadths of the subtended intervals in $\cos\theta_{c.m.}$ ranged from about 0.01 for backward angles at high energies to about 0.12 for counters in the forward hemisphere.

The counter S_0 shown partly around the H₂ target

(Fig. 5) was arranged so as to be missed by pions in the beam, but to be traversed by any pion scattered from the target into a π counter.

It is important to note that each of the π and ρ counters had tunnel-diode pulse output units which delivered pulses of uniform amplitude and shape whenever the photomultiplier outputs exceeded a certain small value. This feature was essential to the valid operation of the matrix coincidence circuit fed by the π and ρ counters.

D. The Electronics System

The scheme of the electronics is shown in Fig. 6. There were three main sections to the system: the monitor section, the matrix coincidence and logic section (enclosed by dashed line in Fig. 6 and labeled "Matrix coincidence system"), and the core storage system (not shown). Not all of the functions of the elements shown in Fig. 6 will be discussed here, but a rudimentary description of their operation follows.

1. Beam Monitor System

Pulses from the monitor counters M_1, M_2, and M_3 were synchronized for beam pions with a resolution time of 2 nsec. Since in the worst case the proton flight time from M_1 to M_3 was 7 nsec longer than the pion time, less than 0.1% of the total monitor counts were due to protons. A "double-pulse-rejection system" was incorporated into the monitor to reject pulses from any pair of charged particles that traversed M_1 and M_2 with less than 40 nsec time separation. So for a pion to register in the monitor system, and thus to qualify to trigger the subsequent matrix system, it could be neither preceded nor followed by another charged particle in M_1M_2 within 40 nsec.

The purpose of the double-pulse-rejection feature was threefold: (a) It limited the acceptance of possible scattering events to only one for each "gate" to the matrix coincidence system (the gate that allowed pulses to enter the matrix was 35 nsec long). (b) It ensured that the number of counts in the monitor system would be equal to those that had the opportunity to be scattered and accepted by the matrix. (c) It functioned so as to reduce the number of accidental counts in the monitor system to a negligible value.

An explanation of this third feature, that is, the reduction of accidentals, is evident from a description of the method of double-pulse rejection. Separate pulses were taken from M_1 and M_2, and each was "stretched" to a length of about 45 nsec and fed into its own discriminator. If two pulses occurred in one of these counters within a time of about 40 nsec, their overlap produced a pulse of such height as to be above the discriminator level and thus induced an output pulse. Whenever both M_1 and M_2 discriminators gave such pulses in coincidence, an "off" gate was imposed upon $M_1M_2M_3$ monitor output. The reduction of monitor

accidental counts can now be understood as follows. Counters M_1 and M_2 were both large enough to include all the beam cross section, so a predominant type of accidental in $M_1M_2M_3$ could have consisted of the close passage of two beam particles, first a proton and then a pion, both of which registered in M_1 and M_2 but with the pion missing M_3, thus allowing a possible false association of an M_3 count (proton) with a coincidence of M_1 and M_2 (pion). But the double-pulse-rejection feature eliminated such a source of accidental associations. Since the counts occurring in M_3 were predominantly due to particles that had traversed M_1 and M_2 (i.e., there was relatively little counting of "ambient" particles), this feature reduced monitor accidentals to a negligible number.

The foregoing characteristics of the monitor counter system were designed to allow the registration of only those single pions that could have been scattered and accepted for analysis by the matrix, logic, and storage systems.

2. Matrix Coincidence and Logic

The triggering of the matrix system, which allowed it to accept counts from the π and ρ arrays, required a count in S_0 (see Fig. 5, above) in coincidence with the $M_1M_2M_3$ condition (M). The resolution time of this $M-S_0$ requirement was 20 nsec: it reduced the duty cycle of the matrix by a factor of about 50 with respect to triggering on M alone, and it ensured that a particle was scattered in the direction of the array of π counters.

Pulses from the π and ρ arrays could enter the matrix if they occurred within 35 nsec of the $M-S_0$ trigger. During the identification of the matrix coincidences between π and ρ pulses, and while they were being checked by the logic system for acceptability as elastic or inelastic events, and finally stored, the matrix was unable to accept additional events: therefore, in these periods the monitor scalers and prescalers were gated "off" so as to maintain a valid monitoring of beam particles that could be scattered and accepted. This "off" gate varied in length from 7 to 100 μsec, depending upon the duration of the "busy" time of the matrix and logic system, and averaged about 20 μsec.

The combination of small groups of ρ counters to form the various P counters, each of which was the elastic proton counter companion to its respective π counter, was accomplished electronically in the section labeled "Adder matrix" in Fig. 6. The various πP pairs provided 21 channels for elastic events at various angles. Inelastic scattering events were sampled by 42 coincidence pairs, two for each π counter, usually formed by the use of each ρ counter adjacent to a given P counter as a coincidence partner with the related π counter. These selected ρ counters are designated by the lines I_nA and I_nB emerging from the adder matrix in Fig. 6, where n refers to the related π_n counter, and n runs from 1 to 21.
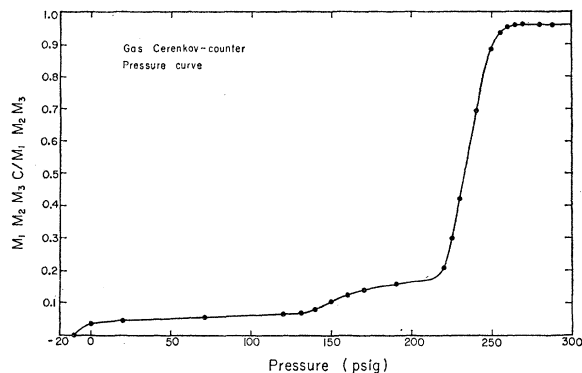
Fig. 7. Gas-Cerenkov-counter pressure curve taken at 698 MeV.

The correction for the inelastic contributions to the elastic channels was estimated by an interpolation and averaging treatment of these "off-elastic" coincidence counts. To each of these off-elastic pairs the output of the associated P counter was added in inverted phase so as to discard from the inelastic counting those cases involving both elastic and inelastic channels simultaneously. This introduced an additional negligible correction.

3. Magnetic Core Storage

The outputs from the 63 channels of elastic and inelastic coincidences were addressed to the various storage locations in the magnetic-core storage of a pulse-height analyzer. If only one of the 63 coincidences in the coincidence matrix system occurred for a given trigger, the event was stored. If there was no coincidence for a given trigger, the trigger was counted in a scaler labeled "zero invalids." If there was more than one coincidence for a given trigger, the trigger was recorded in a scaler labeled ">1 invalids," and the coincidences were not stored in the pulse-height analyzer. The >1 invalids did not occur very frequently, and it is believed that essentially no elastic data were lost as a result of this type of invalid event. After an appropriate length of running time, the number of counts in each of the 63 channels was read out of the pulse-height analyzer on an electric typewriter and punched onto IBM cards simultaneously.

4. Light-Pulser Test System

A system to test all of the electronics as a unit was devised by employing light pulsers attached to each counter and properly timed relative to one another. All possible $\pi-\rho$ counter pairs were pulsed in a systematic manner, along with M_3, S_0, and another counter L, which replaced M_1 and M_2 in the monitor coincidence. Therefore, each time the light pulser was triggered, five counters received pulses. They were L, M_3, S_0, π_k, and ρ_l, where k ranged from 1 to 21, and l ranged from

1 to 25 for each value of k. It required 525 pulses to check all of the π and ρ counter pairs in a complete check cycle. The electronic system was frequently checked for malfunction by running the test system through N cycles, and then examining each of the 63 pulse-height-analyzer outputs to see if it was the correct multiple of N.

Counter voltages were established by use of the light pulsers, the latter having been first standardized in an appropriate manner. The essential requirement was that the photomultiplier output pulses be within such a range as to allow the tunnel-diode output unit from each π and ρ counter to deliver a reasonably uniform pulse whenever a particle passed through the counter.

E. Measurement of Beam Contamination

A gas Čerenkov counter[7] utilizing SF_6 was employed to measure the beam fractions consisting of positrons and muons. During such measurements the counter was inserted into the beam immediately following the H_2 target. This counter, in coincidence with $M_1M_2M_3$, could be made to respond to positrons only, positrons plus muons, or to the total beam of positrons, muons, and pions, by successively increasing its gas pressure. One of the response curves thus generated is shown in Fig. 7.

The analysis of such curves and the results of beam-contamination measurements are discussed in Sec. III B below.

III. ANALYSIS OF DATA

A. The Uncorrected Differential Cross Section

If pion counter π_i subtends a c.m. solid angle Ω_i^* at angle θ_i^* with respect to the incident beam direction at the target, where the c.m. refers to an incident pion and a target proton at rest, then the differential elastic-scattering cross section at angle θ_i^* is given, before corrections, by

$$(d\sigma/d\Omega^*)(\theta_i^*) = R_i/nx\Omega_i^*, \tag{1}$$

where $n=$protons/cm^3 in the LH$_2$, $x=$average path length for beam pion in the LH$_2$, and

$$R_i = \frac{\text{coincidences}(M_1M_2M_3S_0\pi_iP_i)}{\text{coincidences}(M_1M_2M_3)}. \tag{2}$$

The effect of the Mylar walls of the hydrogen vessel was eliminated by the usual empty-target subtraction; so,

$$R_i = R_i{}^{\text{full}} - R_i{}^{\text{empty}}. \tag{3}$$

Each of these R's is evaluated from several "runs"; so, for example,

$$R_i{}^{\text{full}} = \sum_{\alpha=1}^{n} \pi_{i\alpha}{}^{\text{full}} / \sum_{\alpha=1}^{n} M_\alpha, \tag{4}$$

[7] J. Atkinson and V. Perez-Mendez, Rev. Sci. Instr. **30**, 865 (1959).

FIG. 8. Pion-proton elastic kinematic curves showing band where elastic data were collected, two of the 42 regions where inelastic data were collected, and region where reverse-elastic band overlaps elastic band.
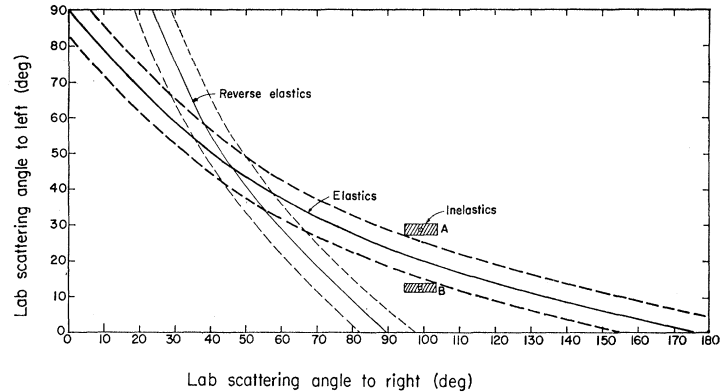
where the index α specifies the run, and we have simplified the expression by writing π_i for the type of coincidence count appearing in the numerator of (2) and M for that in the denominator.

The general requirements of acceptability for the data from the various runs employed the usual tests of a satisfactory relation between the rms deviation from average and the standard deviations calculated from statistics. A rejection criterion for the data from a given run was established as follows. The run α was rejected if:

$$|\text{Res.}|_\alpha > 3(|\text{S.D.}|_\alpha + \text{rms Res.}),$$

where $|\text{Res.}|_\alpha = $ residual of run α, i.e., the deviation of R_α from R, $|\text{S.D.}|_\alpha = $ standard deviation of R_α, rms Res. $=$ root-mean-square residual for all runs of this type, excluding run α. In these expressions we have suppressed the notations referring to channel "i" and to "full" or "empty." We made the assumption that a residual value greater than the magnitude stated indicated a strong probability of instrumental malfunction. Actually, less than 0.1% of the data were rejected because of this criterion.

Since the statistical errors and the deviations from averages showed a satisfactory relationship, the error for the uncorrected differential cross section expressed in (1) was evaluated from the statistics by:

$$\Delta\sigma_i = (1/nx\Omega_i^*)[(\Delta R_i^{\text{full}})^2 + (\Delta R_i^{\text{empty}})^2]^{1/2}, \quad (5)$$

where ΔR_i denotes the standard deviation appropriate to an evaluation of R_i as given in (4). This value of $\Delta\sigma_i$ is subsequently combined with other errors arising from uncertainties in the corrections to be applied.

B. Corrections to the Data

1. Inelastic Scattering

By inelastic scattering we mean an event for which the final state consists of something other than a single pion and a proton. The solid angles of the π and P counters—and their kinematic relationships in defining the elastic channels—suppressed response to inelastic events, but it is necessary to estimate the contribution

in these channels made by inelastic processes. For this purpose the "I-channels" mentioned in Sec. II D 2, consisting of coincidences between π counters and off-elastic ρ counters, were defined.

Figure 8 shows the kinematic relationship between the pion lab angle and the proton lab angle, both for the pion scattered to the right (heavy solid curve), and for the pion scattered to the left (light solid curve). In this experiment elastic events were measured with the pion going to the right. Because of the finite size of both the π and P counters, these kinematic curves are spread out into bands, as indicated by the dashed curves in Fig. 8. Areas A and B in Fig. 8 are defined, for example, by $\pi - \rho$ counter pairs that are outside the elastic bands. Coincidence counts were measured in 42 areas, such as A and B, all of which were in fairly close proximity to the (heavy dashed) elastic band. The 42 ratios of these counts to the beam monitor counts were formed. Each particular ratio was then divided by the product of the lab solid angles of the π and ρ counters contributing to it, thus defining a quantity Z which is the number of inelastic counts per unit monitor count and per unit product of solid angles, for a specific pair of counters.

We then assumed a Z coordinate axis normal to the plane defined in Fig. 8. A surface $Z(x,y)$ was least-squares fitted[8] to the data points in Z by using an equation of the form

$$Z(x,y) = A_0 + A_1(x+y) + A_2xy + A_3(x^2+y^2)$$
$$+ A_4(x^2y+xy^2) + \cdots, \quad (6)$$

where $x = \cos\theta_{\text{right}}$ and $y = \cos\theta_{\text{left}}$. A sufficient number of terms was used to obtain a reasonable fit; usually, it was only those terms up to and including $A_3(x^2+y^2)$. An equation symmetric in x and y was chosen because the inelastic scattering is symmetric with respect to scattering left and right. Powers of $\cos\theta$ were used, rather than powers of θ, in order to make the surface for the region $0 < \theta < 180$ deg agree with the surface for the region $360 > \theta > 180$ deg.

[8] P. Cziffra and M. J. Moravcsik, Lawrence Radiation Laboratory Report UCRL-8523 Rev., 1959 (unpublished).
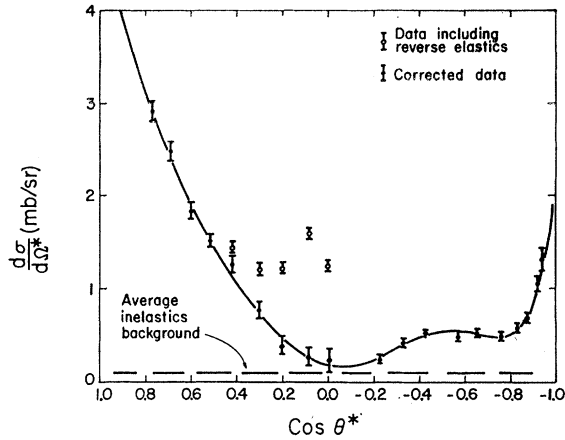
FIG. 9. Differential-cross-section curve for an incident pion lab kinetic energy of 990 MeV, including corrected data points with errors, data points before reverse-elastics correction was applied, and average inelastic background.

The value, Z_i, of Z at the coordinates corresponding to the ith elastic channel point (lying on the heavy solid curve) was determined and then multiplied by the lab solid angles of both the π_i and the P_i counters. The resultant product I_i is the inelastics correction for the ith elastic channel. Equation (1) then becomes

$$(d\sigma/d\Omega^*)(\theta_i^*) = (1/nx\Omega_i^*)(R_i{}^{\text{full}} - R_i{}^{\text{empty}} - I_i) \quad (7)$$

for each elastic channel.

The statistical errors from the inelastic-channel counts (ratios to monitor) provided error values for the data points in Z which were employed in making the least-squares fit to a surface $Z(x,y)$. The error matrix thus determined gave means of assigning an error to Z_i, and thus to I_i. The contribution to the error in differential cross section is made by an additional term in Eq. (5), which now becomes

$$\Delta\sigma_i = (1/nx\Omega_i^*)[(\Delta R_i{}^{\text{full}})^2 + (\Delta R_i{}^{\text{empty}})^2 + (\Delta I_i)^2]^{1/2}. \quad (8)$$

Figure 9 shows the relative magnitudes of the elastic data (solid curve) and the average charged inelastic background (dashed curve) as measured at a pion lab kinetic energy of 990 MeV.

2. Accidental Counts

The high counting rates of the monitor counters (M_1, M_2, M_3) demand careful consideration of the accidental-coincidence component in the monitor counts. Usually the most predominant type of accidental coincidence in a threefold coincidence is one where two of the pulses—e.g., pulses from M_1 and M_2—are definitely related, and the third—e.g., a pulse from M_3—is random. This type of accidental coincidence could have resulted in a considerable ($\approx 4\%$) correction to the monitor counts in this experiment, except for the fact that the monitor system was "protected" against this

type of accidental coincidence by the double-pulse-rejection system. (See Sec. II D 1.) Other types of accidental coincidences in the monitor system were calculated to be negligible.

Accidental coincidences in the elastic and inelastic channels were measured in several cases, including those channels fed by the π and ρ counters with the highest singles counting rate; in all cases it was found that these accidental coincidences were also negligible.

3. "Reverse-Elastic" Scattering

As was previously mentioned, the heavy dashed curves in Fig. 8 indicate the region where elastic data were taken at a particular energy. The region bounded by the light dashed lines is called the reverse-elastics region, because the pion scatters toward the proton counters and the proton recoils toward the pion counters. In the relatively small area where the reverse-elastic band overlaps the elastic band, reverse-elastic counts are recorded in those elastic channels. In this overlap area, the pion counts in a proton counter, say P_k, and the recoil proton counts in the corresponding π_k counter.

Pulses, from π and ρ counters, that resulted from reverse-elastic events could not be eliminated by timing relationships because of the relatively wide (35-nsec) gate to the coincidence matrix system and the "slow" coincidence circuits in the matrix system.

After all other corrections to the $\pi - \rho$ counter matrix data have been applied, the counting rate in a particular elastic channel is the sum of the contribution from elastic events of the desired "forward" type (i.e., pion scatters to the right) and the contribution from reverse-elastic events. This is expressed in the relationship

$$\Omega_f\sigma_0(\theta) = \Omega_f\sigma(\theta) + \Omega_r\sigma(\theta_r), \quad (9)$$

where $\Omega_f =$ solid angle for the forward-elastic channel at angle θ, $\Omega_r =$ solid angle subtended for the reverse-elastic events in this channel, $\sigma_0(\theta) =$ apparent differential cross section at angle θ, uncorrected for reverse-elastic events, $\sigma(\theta) =$ true differential cross section, $\sigma(\theta_r) =$ true differential cross section at the angle θ_r which is the effective pion scattering angle for the reverse-elastic events. From this expression, by rearrangement, we have

$$\sigma(\theta) = \sigma_0(\theta) - (\Omega_r/\Omega_f)\sigma(\theta_r). \quad (10)$$

We attempted to use this relationship to correct the "observed" cross section and to obtain the true cross section, employing in first approximation for $\sigma(\theta_r)$ the observed value at θ_r. The cross-section curve through the data points was then refitted, using this first-corrected value of $\sigma(\theta)$, and an iteration of this procedure continued until a convergence was obtained at a final value for $\sigma(\theta)$.

Actually, the convergence was greatly facilitated by converting (10) into the form

$$\sigma(\theta) = \frac{\Omega_f}{\Omega_f + \Omega_r}\sigma_0(\theta) - \frac{\Omega_r}{\Omega_f + \Omega_r}[\sigma(\theta_r) - \sigma(\theta)]. \quad (11)$$

In the form (11) the correction term is typically much smaller than in (10), and convergence was more directly achieved. As a check on results it was always verified that both forms (10) and (11) were satisfied by the final values of the cross sections. The solid-angle values were calculated with the aid of a computer program that accounted for sizes and positions of counters, size and shape of H_2 target, intensity distribution and momentum distribution in the pion-beam cross section, and convergence of the pion beam.

The error inherent in this correction operation was calculated from the uncertainties in the quantities appearing in Eq. (10), and was incorporated into the errors in the final data for the cross sections. In Fig. 9 an example of the data is shown, for pion energy of 990 MeV, illustrating the magnitude of the reverse-elastics correction in this case.

4. Corrections to Monitor for Beam Contamination

The application of a gas Čerenkov counter for the measurement of muon- and positron-beam contamination was mentioned in Sec. II E. The K^+-meson component was negligible because of its short lifetime. The proton component was successfully rejected by time-of-flight requirements, and its influence upon counting rates was reduced by the velocity-spectrometer action, which eliminated a considerable fraction of the protons from the beam.

Positrons were primarily produced at the Bevatron target from pair production by photons from π^0 decay, and were thus subject to the beam momentum selection and could be readily identified by the Čerenkov counter. Positive muons generated by pion decay in the beam preceding the bending magnet B_2 (Fig. 2) were likewise subject to momentum selection and identified by the Čerenkov counter. Those muons produced between B_2 and the LH$_2$ target, which traverse M_3 and the LH$_2$ target, were evaluated by calculation.

In Fig. 10 we show the fraction of the total monitored beam contributed by these processes at various beam energies. Their scattering in the LH$_2$ target at the angles of concern was so small as to involve no correction in the π and ρ counter data, but only in the monitor data.

5. Miscellaneous Further Corrections

Certain further small corrections were involved, such as: (a) Correction for dead time in counter S_0. (b) Correction for double scattering of pions or protons in the H$_2$ target and walls. (c) Correction for finite angular size of the elastic channel counters. In a few cases where
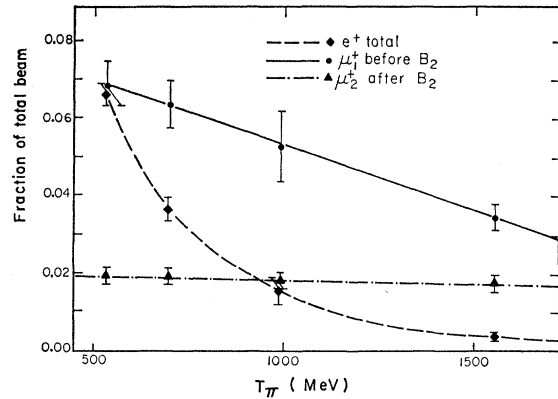

FIG. 10. Muon and electron contamination in pion beam plotted versus incident pion lab kinetic energy.

the cross section was small, but rapidly changing, this was important.

The largest contributions to the quoted errors came from statistics and, for certain points, from the uncertainties in the reverse-elastic correction.

IV. EXPERIMENTAL RESULTS

A. Differential Cross-Section Data

The elastic differential cross sections are listed in the tables in Figs. 11–17, together with the errors (standard deviations) and the cosines of the scattering angles in the c.m. system. The values listed for $\cos\theta^* = 1.0$ were calculated by using dispersion relations.[9]

Although data were taken at 21 different angles at each energy, the data at some of these angles were rejected. At small angles of scattering, the recoil protons did not have enough energy to reach the proton counters. This eliminated the first five angles at 533 MeV, four at 581 MeV, three at 698 MeV, and two at 873 MeV, and one at both 990 and 1311 MeV. The data from channel 11 appeared to have a systematic error of unknown origin; as a result the differential cross sections for this channel were significantly too large at all energies. The probability of such a phenomenon occurring naturally is extremely small, and hence the data from channel 11 were also rejected.

B. Fitting with Power Series in Cosθ*

A curve having the equation

$$d\sigma(\theta^*)/d\Omega^* = \sum_{n=0}^{N} a_n \cos^n\theta^* \quad (12)$$

was least-squares fitted to the data points.[8] The fitted curves, along with the data points, are shown in Figs. 11 through 17. The dispersion-relations point was used to make the final fit at all energies. A fourth-order fit, i.e., $N = 4$, was used at the three lowest energies of this experi-

---

[9] See for example: J. W. Cronin, Phys. Rev. **118**, 824 (1960).
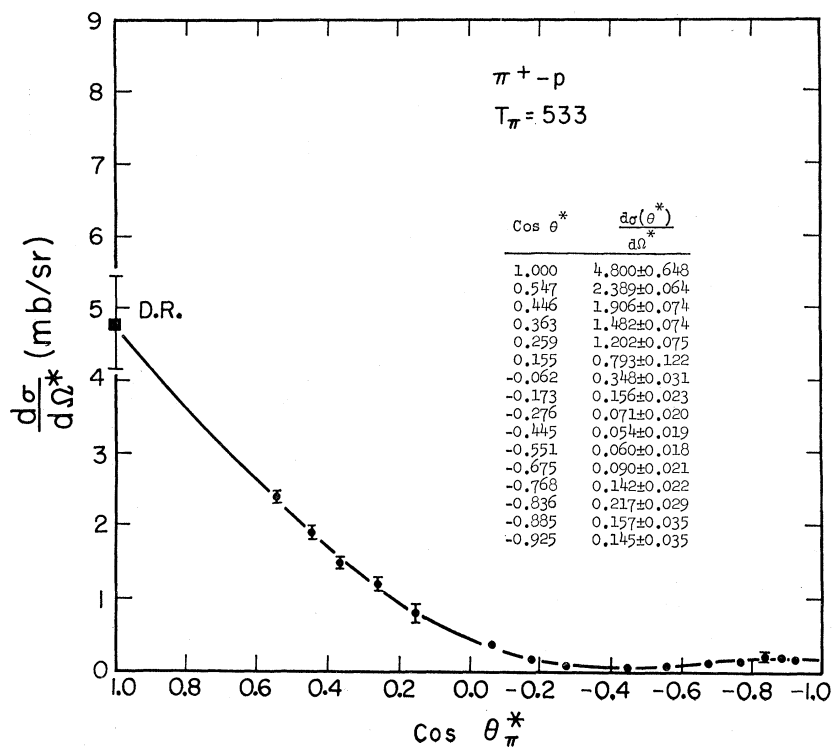
FIG. 11. The $\pi^+ - p$ differential cross-section curve for an incident pion lab kinetic energy of 533 MeV.

Cos θ^*	$\frac{d\sigma(\theta^*)}{d\Omega^*}$
1.000	4.800±0.648
0.547	2.389±0.064
0.446	1.906±0.074
0.363	1.482±0.074
0.259	1.202±0.075
0.155	0.793±0.122
-0.062	0.348±0.031
-0.173	0.156±0.023
-0.276	0.071±0.020
-0.445	0.054±0.019
-0.551	0.060±0.018
-0.675	0.090±0.021
-0.768	0.142±0.022
-0.836	0.217±0.029
-0.885	0.157±0.035
-0.925	0.145±0.035

FIG. 12. The $\pi^+ - p$ differential cross-section curve for an incident pion lab kinetic energy of 581 MeV.

Cos θ^*	$\frac{d\sigma(\theta^*)}{d\Omega^*}$
1.000	3.470±0.742
0.613	2.163±0.056
0.533	2.032±0.054
0.429	1.512±0.071
0.345	1.019±0.082
0.239	0.807±0.091
0.135	0.589±0.131
-0.083	0.259±0.022
-0.193	0.086±0.019
-0.295	0.020±0.019
-0.461	0.046±0.018
-0.565	0.090±0.017
-0.686	0.127±0.018
-0.776	0.156±0.019
-0.842	0.113±0.022
-0.890	0.153±0.023
-0.928	0.079±0.028

FIG. 13. The $\pi^+ - p$ differential cross-section curve for an incident pion lab kinetic energy of 698 MeV.

Cos θ^*	$\frac{d\sigma(\theta^*)}{d\Omega^*}$
1.000	2.250±0.542
0.664	1.426±0.050
0.583	1.221±0.044
0.499	1.041±0.046
0.391	0.694±0.043
0.303	0.607±0.049
0.195	0.375±0.050
0.089	0.156±0.072
-0.129	0.130±0.026
-0.237	0.113±0.021
-0.336	0.115±0.023
-0.497	0.208±0.025
-0.596	0.264±0.022
-0.710	0.267±0.023
-0.794	0.272±0.027
-0.855	0.195±0.032
-0.899	0.239±0.035
-0.934	0.186±0.045

FIG. 14. The $\pi^+ - p$ differential cross-section curve for an incident pion lab kinetic energy of 873 MeV.

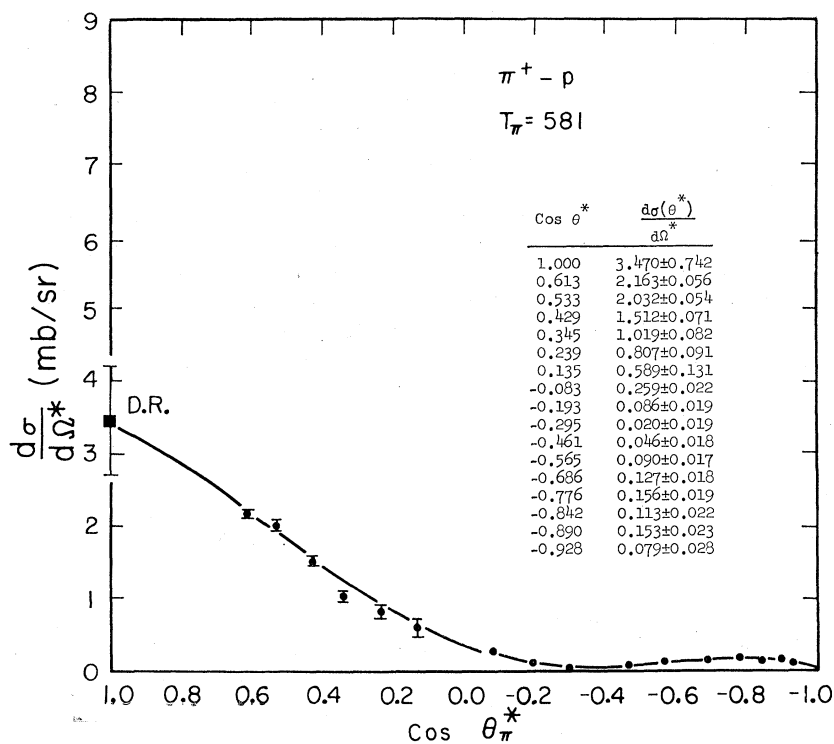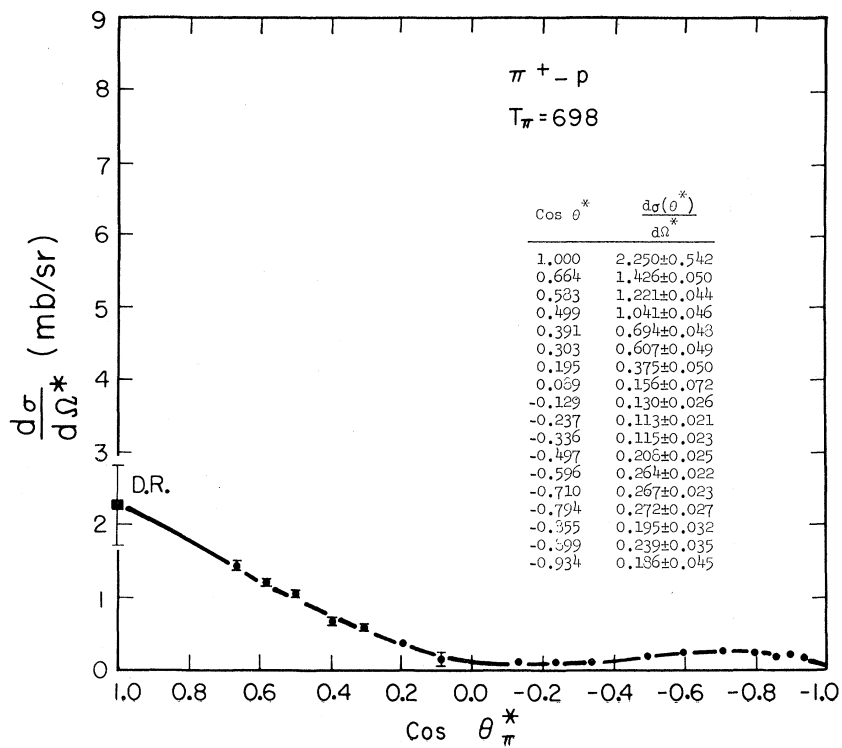| Cos θ^*	$\frac{d\sigma(\theta^*)}{d\Omega^*}$
1.000	3.800±0.453
0.709	2.339±0.081
0.627	1.788±0.072
0.540	1.549±0.065
0.450	1.279±0.066
0.336	0.854±0.103
0.246	0.551±0.103
0.134	0.278±0.090
0.027	0.254±0.116
-0.190	0.141±0.039
-0.295	0.095±0.041
-0.391	0.172±0.042
-0.542	0.265±0.046
-0.635	0.397±0.047
-0.740	0.385±0.045
-0.816	0.447±0.053
-0.871	0.413±0.063
-0.910	0.575±0.069
-0.942	0.854±0.100

Fig. 15. The $\pi^+ - p$ differential cross-section curve for an incident pion lab kinetic energy of 990 MeV.

$\pi^+ - p$
$T_\pi = 990$

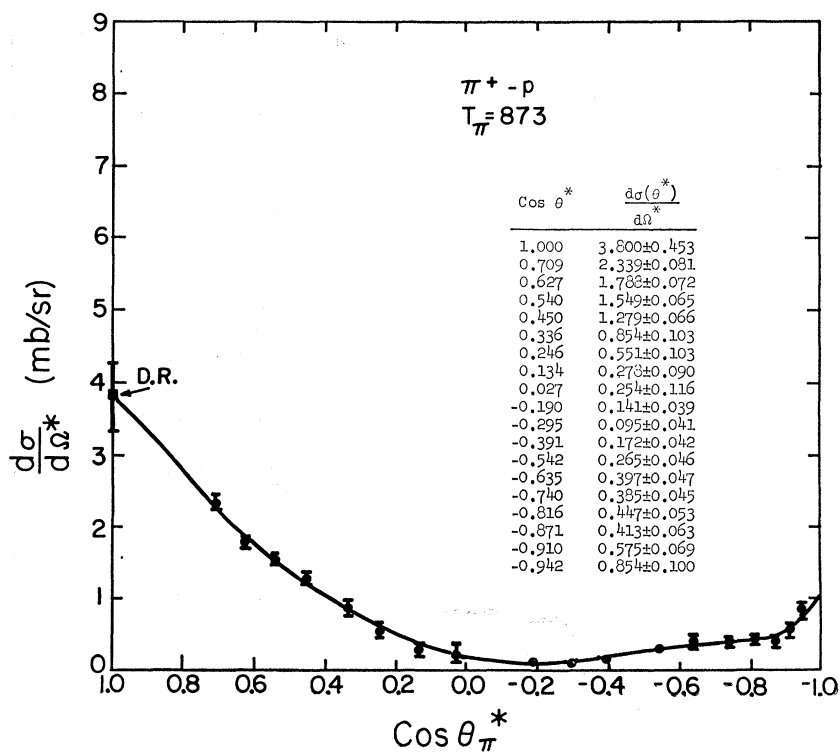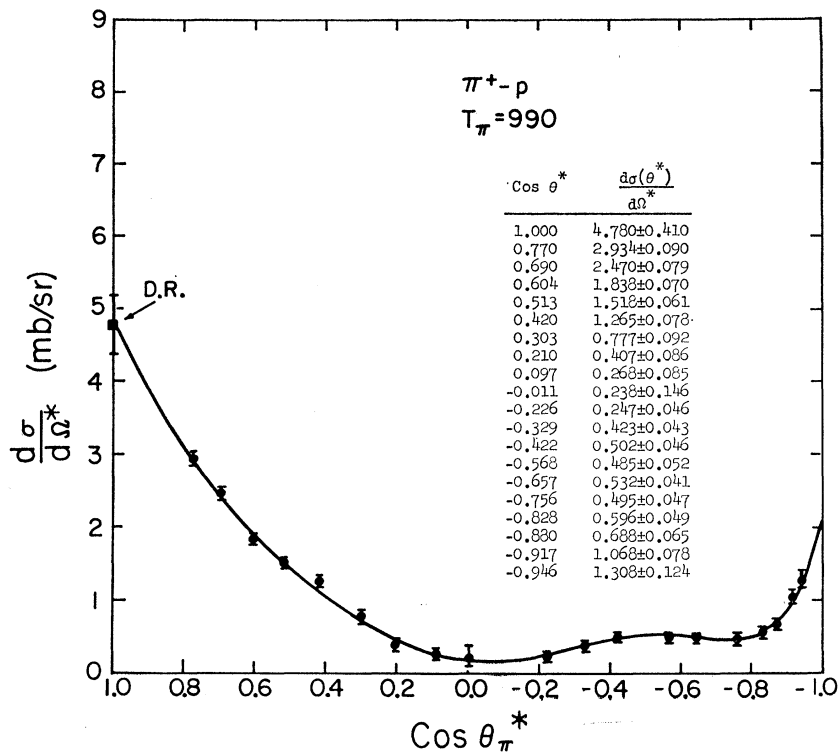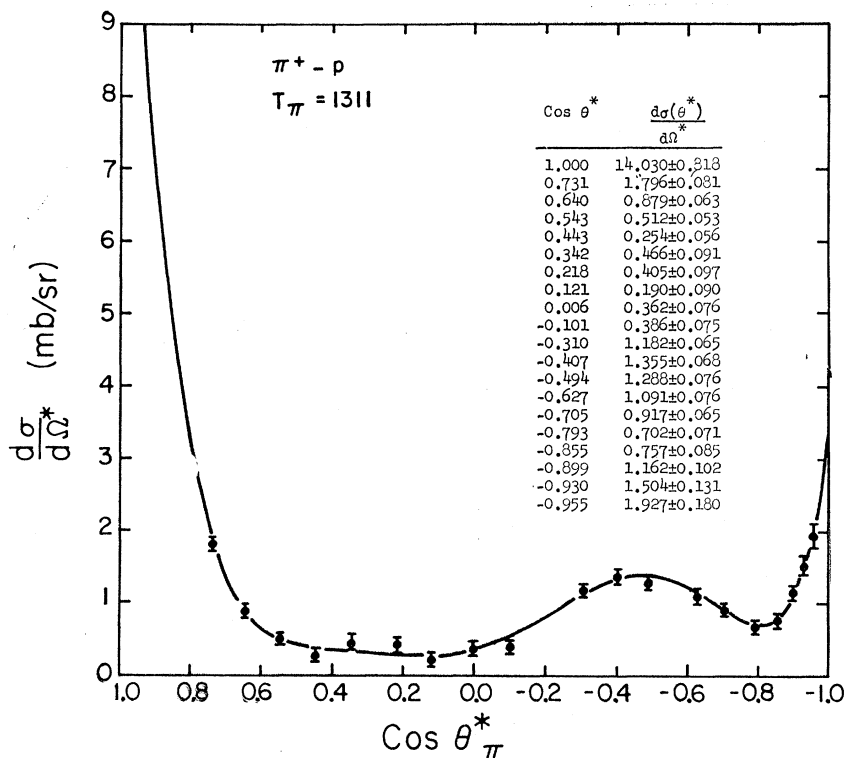| Cos θ^*	$\dfrac{d\sigma(\theta^*)}{d\Omega^*}$
1.000	4.780±0.410
0.770	2.934±0.090
0.690	2.470±0.079
0.604	1.838±0.070
0.513	1.518±0.061
0.420	1.265±0.078
0.303	0.777±0.092
0.210	0.407±0.086
0.097	0.268±0.085
-0.011	0.238±0.146
-0.226	0.247±0.046
-0.329	0.423±0.043
-0.422	0.502±0.046
-0.568	0.485±0.052
-0.657	0.532±0.041
-0.756	0.495±0.047
-0.828	0.596±0.049
-0.880	0.688±0.065
-0.917	1.068±0.078
-0.946	1.308±0.124

Fig. 16. The $\pi^+ - p$ differential cross-section curve for an incident pion lab kinetic energy of 1311 MeV.

$\pi^+ - p$
$T_\pi = 1311$

Cos θ^*	$\dfrac{d\sigma(\theta^*)}{d\Omega^*}$
1.000	14.030±0.818
0.731	1.796±0.081
0.640	0.879±0.063
0.543	0.512±0.053
0.443	0.254±0.056
0.342	0.466±0.091
0.218	0.405±0.097
0.121	0.190±0.090
0.006	0.362±0.076
-0.101	0.386±0.075
-0.310	1.182±0.065
-0.407	1.355±0.068
-0.494	1.288±0.076
-0.627	1.091±0.076
-0.705	0.917±0.065
-0.793	0.702±0.071
-0.855	0.757±0.085
-0.899	1.162±0.102
-0.930	1.504±0.131
-0.955	1.927±0.180
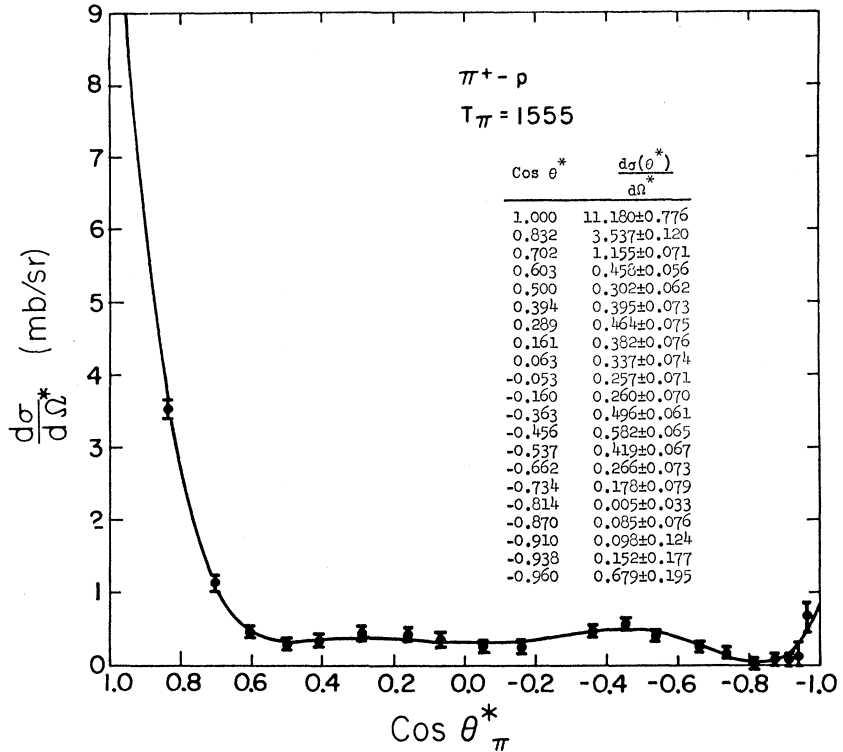
FIG. 17. The $\pi^+ - p$ differential cross-section curve for an incident pion lab kinetic energy of 1555 MeV.

$$\pi^+ - p$$
$$T_\pi = 1555$$

Cos θ^*	$\dfrac{d\sigma(\theta^*)}{d\Omega^*}$
1.000	11.180±0.776
0.832	3.537±0.120
0.702	1.155±0.071
0.603	0.458±0.056
0.500	0.302±0.062
0.394	0.395±0.073
0.289	0.464±0.075
0.161	0.382±0.076
0.063	0.337±0.074
-0.053	0.257±0.071
-0.160	0.260±0.070
-0.363	0.496±0.061
-0.456	0.582±0.065
-0.537	0.419±0.067
-0.662	0.266±0.073
-0.734	0.178±0.079
-0.814	0.005±0.033
-0.870	0.085±0.076
-0.910	0.098±0.124
-0.938	0.152±0.177
-0.960	0.679±0.195

ment; a seventh-order fit was used at the four highest energies.

The determination of the correct order of fit to be used is a rather difficult problem. One criterion accepted was that if a kth-order fit is needed at some particular energy, then at higher energies the order of fit should never be less than k. The basis for this criterion is that if a specific lth partial wave is needed at a certain energy, this lth partial wave should also be present at all higher energies, even though its contribution may be very small. Another, and an important criterion, was to choose that order of fit that gave the best agreement between the curves fitted with and without the dispersion-relations point.[9]

At 873 MeV the data could statistically be fitted, i.e., with satisfactory χ^2, with a third-order expression.

However, a third-order fit did not produce the sharp rise at $\cos\theta^* = -1$, as indicated by the data points. A seventh-order fit was the lowest order fit, made without the dispersion-relations point, that both produced the sharp rise at $\cos\theta^* = -1$ and also had the correct value at $\cos\theta^* = +1$. This sharp rise at $\cos\theta^* = -1$ becomes more pronounced at 990 MeV, very pronounced at 1311 MeV, and starts to diminish again at 1555 MeV.

The standard statistical tests, such as the χ^2 test and the Fisher "F" test,[8] were taken into consideration, but they were sometimes misleading. Figure 18 shows the values of $(\chi^2/d)^{1/2}$, the "goodness-of-fit" parameter, plotted versus the order of fit N. These plots are for the lowest energy, 533 MeV, and the highest energy, 1555 MeV, where d is the number of degrees of freedom; i.e.,

$$d = P - (N+1), \qquad (13)$$

TABLE I. Values of χ^2, $(\chi^2/d)^{1/2}$, the number of data points,[a] the number of degrees of freedom, and the total elastic cross section with its error at each energy of the experiment.

Energy (MeV)	χ^2	$(\chi^2/d)^{1/2}$	Number of data points	Degrees of freedom	Elastic cross section
533	7.89	0.85	16	11	15.32±0.47
581	25.26	1.45	17	12	12.17±0.57
698	9.28	0.84	18	13	8.02±0.22
873	13.96	1.13	19	11	12.05±0.45
990	11.33	0.97	20	12	14.54±0.31
1311	16.92	1.19	20	12	19.31±0.61
1555	8.36	0.80	21	13	13.04±0.28

[a] The dispersion-relations point, having been used in the curve fitting, is included in the number of data points.
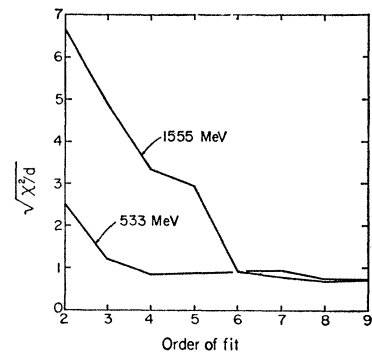
FIG. 18. Curves showing goodness-of-fit parameter $(\chi^2/d)^{1/2}$ plotted versus order of fit for the lowest and highest energies of the experiment.

TABLE II. Coefficients of powers of $\cos\theta^*$.

| Coefficients | Incident pion lab kinetic energy (MeV) | | | | | | |
	533	581	698	873	990	1311	1555
a_0	0.436 ± 0.017	0.336 ± 0.026	0.173 ± 0.014	0.190 ± 0.053	0.184 ± 0.046	0.337 ± 0.052	0.308 ± 0.031
a_1	2.042 ± 0.070	1.745 ± 0.121	0.692 ± 0.049	1.108 ± 0.213	0.528 ± 0.175	-1.266 ± 0.290	0.467 ± 0.175
a_2	2.869 ± 0.101	2.679 ± 0.139	1.960 ± 0.092	3.004 ± 0.621	4.583 ± 0.508	5.272 ± 0.626	1.642 ± 0.397
a_3	0.250 ± 0.250	-0.051 ± 0.377	0.432 ± 0.141	-0.932 ± 1.688	0.920 ± 1.335	-1.235 ± 2.248	-6.322 ± 1.326
a_4	-0.868 ± 0.239	-1.303 ± 0.369	-0.940 ± 0.174	-2.219 ± 1.820	-6.515 ± 1.430	-17.364 ± 1.970	-7.837 ± 1.286
a_5	$\cdots$	$\cdots$	$\cdots$	4.476 ± 3.939	3.607 ± 2.998	10.548 ± 5.072	16.012 ± 2.990
a_6	$\cdots$	$\cdots$	$\cdots$	1.480 ± 1.387	5.237 ± 1.111	20.410 ± 1.764	12.252 ± 1.140
a_7	$\cdots$	$\cdots$	$\cdots$	-3.301 ± 2.611	-3.682 ± 1.978	-2.614 ± 3.415	-4.971 ± 2.068

P being the number of data points to which the curve is fitted.

Figure 18 seems to indicate that a sixth-order fit is sufficient at 1555 MeV, however, a seventh-order fit was chosen because that is the order of fit needed at a lower energy, 873 MeV.

Table I gives the values of χ^2 and $(\chi^2/d)^{1/2}$ for the chosen fit at each energy.

The values of the coefficients a_n and their errors are listed in Table II, and are shown plotted in Fig. 19 with pion lab kinetic energy as the abscissa.

C. Total Elastic Cross Sections

The total elastic cross sections, obtained from the data for differential elastic cross sections by integrating
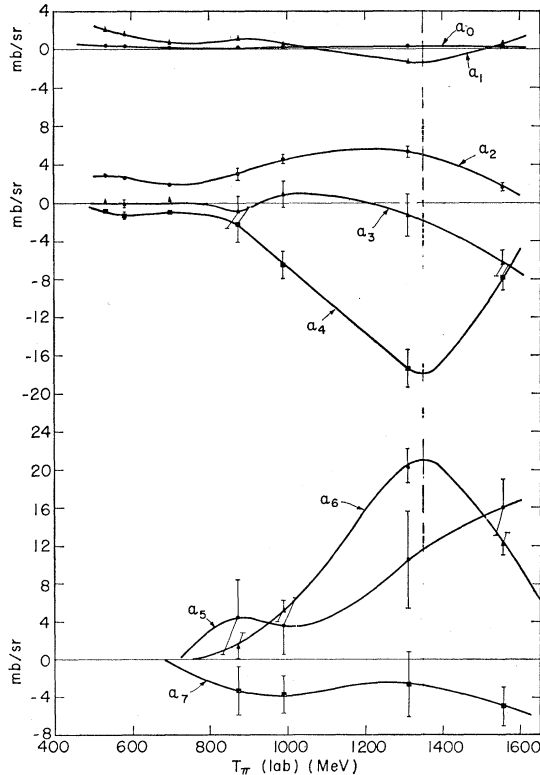

FIG. 19. Coefficients of power series in $\cos\theta^*$ plotted versus the incident pion lab kinetic energy.

under the fitted curves, are listed in Table I, along with their errors. Figure 20 shows the total elastic cross section, the total cross section,[1] and the total inelastic cross section—the last being simply the difference between the first two.

V. DISCUSSION

The major objective of the experiment was to infer the quantum numbers of the state in "resonance" at the pion kinetic energy of 1350 MeV. Secondarily, we hoped to obtain some information concerning the nature of the state contributing to the "shoulder" in the total cross-section curve for pion energy near 850 MeV.

Cursory examination of the differential cross-section curves at various energies (Figs. 11–17) allows the following qualitative observations: The curves for the three lowest energies are of simple and similar shapes, for the three highest energies a more complicated shape is apparent, and for 873 MeV the curve suggests a transition between these two regimes. The characteristic shape of the curves for the three highest energies suggests a substantial contribution with a $[P_3(\cos\theta^*)]^2$ dependence, which could be produced by a prominent amplitude in the $l=3$ orbital state.

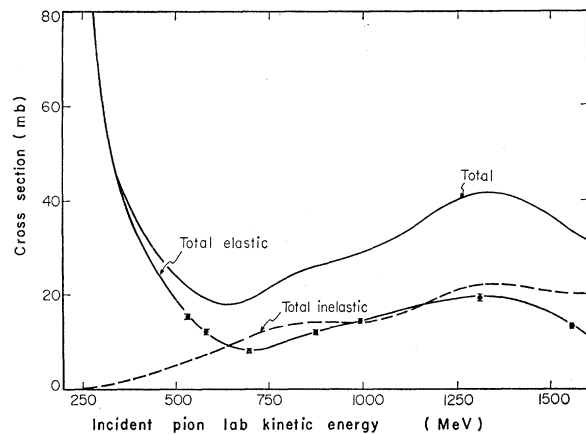A much stronger basis for interpretation is provided by the plots of the behavior of the coefficients of the

FIG. 20. The π^+-p total cross section, total elastic cross section, and total inelastic cross section plotted versus incident pion lab kinetic energy.

powers of $\cos\theta^*$ in the power-series expansions of the various curves. The energy dependence of these coefficients is shown in Fig. 19. The interpretation is facilitated by expressing these coefficients in terms of the partial-wave scattering amplitudes by the following operations.

The differential cross section in terms of the partial-wave amplitude is:

$$d\sigma(\theta^*)/d\Omega^* = |\sum_{l=0}^{L} [(l+1)A_l^+ + lA_l^-]P_l(\cos\theta^*)|^2$$
$$+ |\sum_{l=0}^{L} [A_l^+ - A_l^-]P_l^1(\cos\theta^*)|^2, \quad (14)$$

where $A_l^\pm$ is the scattering amplitude for the state of total angular momentum $J = l \pm \frac{1}{2}$. The value of L is the largest value of l needed to fit a particular cross-section curve that the expression is to describe. The amplitudes are expressible in terms of the phase shifts by the form

$$A_l^\pm = [b^\pm \exp(2i\delta_l^\pm) - 1]/2ik, \quad (15)$$

where k is the c.m. wave number for the pion, $\delta_l^\pm$ is the real part of the phase shift, and $b_l^\pm = \exp(-2\beta_l^\pm)$ is the absorption parameter arising from the imaginary part, $\beta_l^\pm$, of the complex phase shift of $\delta + i\beta$.

We now expand Eq. (14) into an expression in powers of $\cos\theta^*$, and for convenience employ the standard symbols S, P, D, F, G, for the scattering amplitudes corresponding to $l=0$, 1, 2, 3, 4, respectively; thus $A_3^+ = F_{7/2}$, and $A_3^- = F_{5/2}$. With this notation, Eq. (14) becomes

$$\frac{d\sigma(\theta^*)}{d\Omega^*} = [S_{1/2}^2 - 2S_{1/2}D_{3/2} - 3S_{1/2}D_{5/2} + P_{1/2}^2 - 2P_{1/2}P_{3/2} - 3P_{1/2}F_{5/2} + 3P_{1/2}F_{7/2} + P_{3/2}^2 + 3P_{3/2}F_{5/2} - 3P_{3/2}F_{7/2}$$

$$+ D_{3/2}^2 + 3D_{3/2}D_{5/2} + (9/4)D_{5/2}^2 + (9/4)F_{5/2}^2 - (9/2)F_{5/2}F_{7/2} + (9/4)F_{7/2}^2]$$

$$+ \cos\theta^*[2S_{1/2}P_{1/2} + 4S_{1/2}P_{3/2} - 9S_{1/2}F_{5/2} - 12S_{1/2}F_{7/2} + 4P_{1/2}D_{3/2} - 9P_{1/2}D_{5/2}$$

$$- 10P_{3/2}D_{3/2} + 21D_{3/2}F_{7/2} + (45/2)D_{5/2}F_{5/2} + 9D_{5/2}F_{7/2}]$$

$$+ \cos^2\theta^*[6S_{1/2}D_{3/2} + 9S_{1/2}D_{5/2} + 6P_{1/2}P_{3/2} + 9P_{1/2}F_{5/2} - 30P_{1/2}F_{7/2} + 3P_{3/2}^2 - 36P_{3/2}F_{5/2}$$

$$- 6P_{3/2}F_{7/2} + 3D_{3/2}^2 - 36D_{3/2}D_{5/2} - (9/2)D_{5/2}^2 - (9/2)F_{5/2}^2 + (207/2)F_{5/2}F_{7/2} + (45/4)F_{7/2}^2]$$

$$+ \cos^3\theta^*[15S_{1/2}F_{5/2} + 20S_{1/2}F_{7/2} + 15P_{1/2}D_{5/2} + 18P_{3/2}D_{3/2} + 12P_{3/2}D_{5/2} + 12D_{3/2}F_{5/2}$$

$$- 110D_{3/2}F_{7/2} - 117D_{5/2}F_{5/2} - 30D_{5/2}F_{7/2}]$$

$$+ \cos^4\theta^*[35P_{1/2}F_{7/2} + 45P_{3/2}F_{5/2} + 25P_{3/2}F_{7/2} + 45D_{3/2}D_{5/2}$$

$$+ (45/4)D_{5/2}^2 + (45/4)F_{5/2}^2 - (675/2)F_{5/2}F_{7/2} - (165/4)F_{7/2}^2]$$

$$+ \cos^5\theta^*[105D_{3/2}F_{7/2} + (225/2)D_{5/2}F_{5/2} + 45D_{5/2}F_{7/2}]$$

$$+ \cos^6\theta^*[(525/2)F_{5/2}F_{7/2} + (175/4)F_{7/2}^2]. \quad (16)$$

Since the scattering amplitudes are complex quantities, complex multiplication must be used in this equation. For example, $F_{7/2}^2$ means $|F_{7/2}|^2$ and $F_{5/2}F_{7/2}$ means the real part of $F_{5/2}^*F_{7/2}$.

In the foregoing expansion we have retained only terms through $l=3$, even though at some energies we tentatively included terms through $\cos^7\theta^*$ in fitting the curves. In such cases, however, the errors in the values of a_7 were large (see Table II). It is our belief that the presence of a small amount of $\cos^7\theta^*$, if it should in fact be considered as required, is due to the superposition of a large F amplitude with a very small onset of the G amplitude. Subsequent interpretations will assume all amplitudes above F to be small.

Due to the complex character of the amplitudes, there are actually 14 amplitude parameters represented in the seven amplitude symbols $S_{1/2}$, $\cdots$, $F_{7/2}$. Thus it is in principle impossible to determine the amplitudes by equating the experimental values for a_0, a_1, $\cdots$, a_7, respectively, to the expressions for these coefficients in Eq. (16). Additional information, e.g., polarization data and the values of elastic and total cross sections, will be required.

But in the absence of a sufficient number of constraints to determine rigidly the amplitude parameters we may still make strong inferences as follows. The dominant features of the plots of the energy dependence of the coefficients in Fig. 19 are the pronounced positive peaking of a_6 and negative peaking of a_4 in the vicinity of the 1350-MeV resonance. Reference to Eq. (16) shows that both these features are promoted by either the $F_{7/2}^2$ term or the $F_{5/2}F_{7/2}$ term. Upon the basis of the small magnitudes of the four lowest coefficients—a_0, $\cdots$, a_3—we assume that terms in the expression for a_4 other than $F_{5/2}F_{7/2}$ and $F_{7/2}^2$ are relatively negligible. And now, by equating the expression for a_6 to 21 mb/sr,

and that for a_4 to -18 mb/sr, as shown in Fig. 19, we calculate that $F_{7/2}{}^2$ is 30 times the magnitude of $F_{5/2}F_{7/2}$. We thus infer that the peak at the pion energy of 1350 MeV is related to an $F_{7/2}$ resonance.

It is necessary, however, to recognize the Minami ambiguity,[10] which expresses the fact that differential cross sections are unchanged if for each value of J we interchange the values of the two scattering amplitudes related to the two values of l contributing. Thus the simultaneous interchange of $S_{1/2}$ with $P_{1/2}$, $P_{3/2}$ with $D_{3/2}$, $D_{5/2}$ with $F_{5/2}$, and $F_{7/2}$ with $G_{7/2}$ will leave $d\sigma/d\Omega$ unaffected. So, although we have adduced evidence for a state with $J = 7/2$, we yet need to provide a basis for choice of parity.

There are at least two reasons for suggesting the $F_{7/2}$ assignment over $G_{7/2}$. First, if the 1350-MeV resonance is a true elastic resonance analogous to the $(\frac{3}{2},\frac{3}{2})$ resonance, i.e., there is an intermediate state consisting of a single particle, it is reasonable to assume that this intermediate particle is an excited nucleon, and hence should have the same parity as the nucleon. It is the $F_{7/2}$ $\pi - N$ state that has positive parity. Another reason for tentatively favoring the $F_{7/2}$ assignment is that it agrees with the Regge-pole formalism as presented by Chew and Frautschi.[11] They would predict that the 1350-MeV resonance has the same parity as the $(\frac{3}{2},\frac{3}{2})$ resonance, which again is positive.

There does not appear to be any single state that is very prominent at the shoulder near 850 MeV. The total elastic and inelastic cross sections are plotted in Fig. 20. The behavior of the total inelastic cross section near 850 MeV is similar to that needed in the Ball-Frazer[5] explanation of peaks in total cross sections. In view of these facts, it can be suggested that the shoulder near 850 MeV is the result of an inelastic enhancement rather than an elastic resonance. It is possible that this inelastic process, which produces the shoulder near 850 MeV in the $T = \frac{3}{2}(\pi^+ - p)$ total cross section, is the same inelastic process that contributes to the $\pi^- - p$ peak at 900 MeV.[1,2] In this case we would suggest $D_{5/2}$, as discussed in the succeeding paper. In fact, although the evidence is not compelling, the alternating signs in the values of a_1, a_3, a_5, and a_7 in Fig. 19 at 850 MeV are consistent with the interference of a $D_{5/2}$ amplitude with F state amplitudes, as may be seen by reference to Eq. (16).

ACKNOWLEDGMENTS

[10] S. Minami, Progr. Theoret. Phys. (Kyoto) **11**, 213 (1954).
[11] G. F. Chew and S. C. Frautschi, Phys. Rev. Letters **8**, 41 (1962).